

# Using high spatial resolution satellite imagery for mapping powdery mildew at a regional scale

Lin Yuan<sup>1</sup> · Ruiliang Pu<sup>4</sup> · Jingcheng Zhang<sup>2</sup> ·  
Jihua Wang<sup>3</sup> · Hao Yang<sup>3</sup>

Published online: 13 November 2015  
© Springer Science+Business Media New York 2015

**Abstract** Efficient crop protection management requires timely detection of diseases. The rapid development of remote sensing technology provides a possibility of spatial continuous monitoring of crop diseases over a large area. In this study, to monitor powdery mildew in winter wheat in an area where a severe disease infection occurred, the capability of high resolution (6 m) multi-spectral satellite imagery, SPOT-6, in disease mapping was assessed and validated using field survey data. Based on a rigorous feature selection process, five disease sensitive spectral features: green band, red band, normalized difference vegetation index, triangular vegetation index, and atmospherically-resistant vegetation index were selected from a group of candidate spectral features/variables. A spectral correction was processed on the selected features to eliminate possible baseline effect across different regions. Then, the disease mapping method was developed based on a spectral angle mapping technique. By validating against a set of field survey data, an overall mapping accuracy of 78 % and kappa coefficient of 0.55 were achieved. Such a moderate but practically acceptable accuracy suggests that the high resolution multi-spectral satellite image data would be of great potential in crop disease monitoring.

**Keywords** Powdery mildew · Winter wheat · Spectral angle mapping (SAM) · SPOT-6

---

✉ Jingcheng Zhang  
zhangjc\_rs@163.com

<sup>1</sup> School of Information Engineering and Art and Design, Zhejiang University of Water Resources and Electric Power, Hangzhou 310018, China

<sup>2</sup> College of Life Information Science and Instrument Engineering, Hangzhou Dianzi University, Hangzhou 310018, China

<sup>3</sup> Beijing Research Center for Information Technology in Agriculture, Beijing Academy of Agriculture and Forestry Sciences, Beijing 100097, China

<sup>4</sup> School of Geosciences, University of South Florida, Tampa, FL 33620, USA

## Introduction

Wheat diseases are important biotic stressors that threaten winter wheat production worldwide (Mahlein et al. 2012). Disease management is usually a costly component in wheat production. Using large amounts of pesticide not only increases the cost of crop production but also causes a potential risk to field environment and eco-system. Large-scale wheat cropping would benefit from a timely and location-specific monitoring system to reduce costs and risks associated with pesticide spray (Lee et al. 2010). Recently, with development of precision agricultural technology, sprayer control systems (e.g., TeeJet 854 Sprayer Control, TeeJet Technologies, Glendale Heights, IL, USA) with variable rate control capability have been applied in agricultural management. In such a variable rate spray system, a key component is to create an accurate prescription map. However, there exist obvious defects associated with conventional disease field scouting approaches, such as subjectivity, low efficiency and spatial limitation. Thus, the spatial continuous feature of remote sensing technology makes it a suitable alternative for producing a prescription map for the pesticide spray application (Sankaran et al. 2010).

The response of electromagnetic radiation interaction with plants due to disease infection serves as a theoretical basis for remote sensing detection (Lee et al. 2010). Basically, infection of a disease pathogen leads to colored spots/lesions on plant organs (e.g., leaves, stems and spike), destruction of pigment systems (mainly chlorophyll), collapse of foliar cellular structure and variation of canopy morphology. All the biophysical alterations as stated above would finally affect the absorption rate in the visible region and the reflective and scattering magnitude in the near infrared (NIR) region, which thus determine spectral characteristics of plants suffering from a specific disease.

A number of studies aiming at identifying the most efficient spectral bands or vegetation indices (VIs) have been conducted at a foliar or canopy level for mapping and monitoring several important crop diseases (e.g., yellow rust, powdery mildew in winter wheat; late blight in tomato) (Wang et al. 2008; Moshou et al. 2011; Zhang et al. 2012). These studies mostly rely on using airborne/satellite images (Franke and Menz 2007; Huang et al. 2007; Calderón et al. 2013). Hyperspectral imagery has exhibited advantages in disease mapping. For instance, Huang et al. (2007) and Zhang et al. (2003) demonstrated that airborne hyperspectral and multi-spectral imagery could be used to detect yellow rust in winter wheat and late blight infestations in tomato fields, respectively. However, the high cost and low availability of hyperspectral image data, as well as difficulties in data collection and data processing, hamper its application in practice. Instead, the relatively low cost and high availability of high resolution multi-spectral images make them reasonable remote sensing surrogates for crop disease mapping. For example, Hicke and Logan (2009) demonstrated the potential of using high spatial resolution satellite imagery in mapping whitebark pine mortality caused by a mountain pine beetle outbreak. Using Worldview-2 sensor data in predicting bronze bug damage in plantation forests, Oumar and Mutanga (2012) also proved their applicability in disease monitoring. As an important fungal disease in winter wheat, powdery mildew (*Blumeria graminis*) causes an obvious foliar symptom that offers the possibility of being detected by remote sensing sensors. The powdery mildew disease spreads quickly in winter wheat fields under suitable weather conditions, and thus monitoring it is important for wheat production. For this case, an attempt to use multi-temporal moderate resolution satellite images in mapping powdery mildew of winter wheat at a regional scale was conducted by Zhang et al. (2014), which achieved an overall accuracy of 78 %. However, because of the patchy characteristic of wheat fields in some regions, it

is necessary to test the potential of using high resolution imagery to monitor plant disease at the field level. To date, only a few studies have been conducted to evaluate the performance of these high resolution data in crop disease mapping. Among various types of multi-spectral images, SPOT-6 provides a new generation of image products, which have high resolution (6 m) and commonly-used setting of bands over visible and NIR spectral regions (Table 1). Given that SPOT-6 has a short revisit time (1–3 days), a wide swath (60 km) and low price, the SPOT-6 data are of great potential to be used in mapping crops at a regional scale. Therefore, the objectives of this study were to: (1) investigate the capability of high spatial resolution multi-spectral remote sensing data (SPOT-6) in mapping powdery mildew-infected wheat areas at a regional scale; (2) evaluate the feasibility of a method associated with a spectral correction (which was processed on the selected features to eliminate possible baseline effects across different regions) and spectral angle mapping (SAM) in crop disease mapping. Relevant issues on feature selection and disease mapping with multi-spectral data were also discussed.

## Materials and methods

### Overall workflow of powdery mildew mapping

Figure 1 presents a workflow of mapping powdery mildew with high-resolution satellite images using the SAM algorithm. To ensure the effectiveness of SFs that would be used for mapping powdery mildew, an experiment on analyzing the spectral response of the disease was conducted separately at the canopy level (see processing procedures in the right branch in Fig. 1). The hyperspectral spectra were measured and converted to broad-band spectra according to a relative spectral response function (RSR function) of the SPOT-6 sensor. The most sensitive SFs to powdery mildew were identified through an independent *t* test and were then used for mapping the disease. A spectral correction was processed on the selected features to eliminate possible baseline effects across different regions. The corrected spectral features were used as a spectral reference of the disease for classification. Finally, both field survey data about disease occurrence and a corresponding high-resolution satellite image were acquired to evaluate the performance of the proposed disease mapping protocol.

### Study area

The canopy level experiment was conducted in an experimental field in Beijing Academy of Agriculture and Forestry Sciences, China (39°56'N, 116°16'E). Cultivar 'Jingdong 8' was chosen as it is moderately susceptible to powdery mildew. During the 2012–2013

**Table 1** Parameters of SPOT-6 imagery

Items	Information
Spatial resolution (m)	6
Multi-spectral bands (nm)	Band 1 (455–525 nm); Band 2 (530–590 nm); Band 3 (625–695 nm); Band 4 (760–890 nm)
Image swath (km)	60
Revisit time (day)	1–3

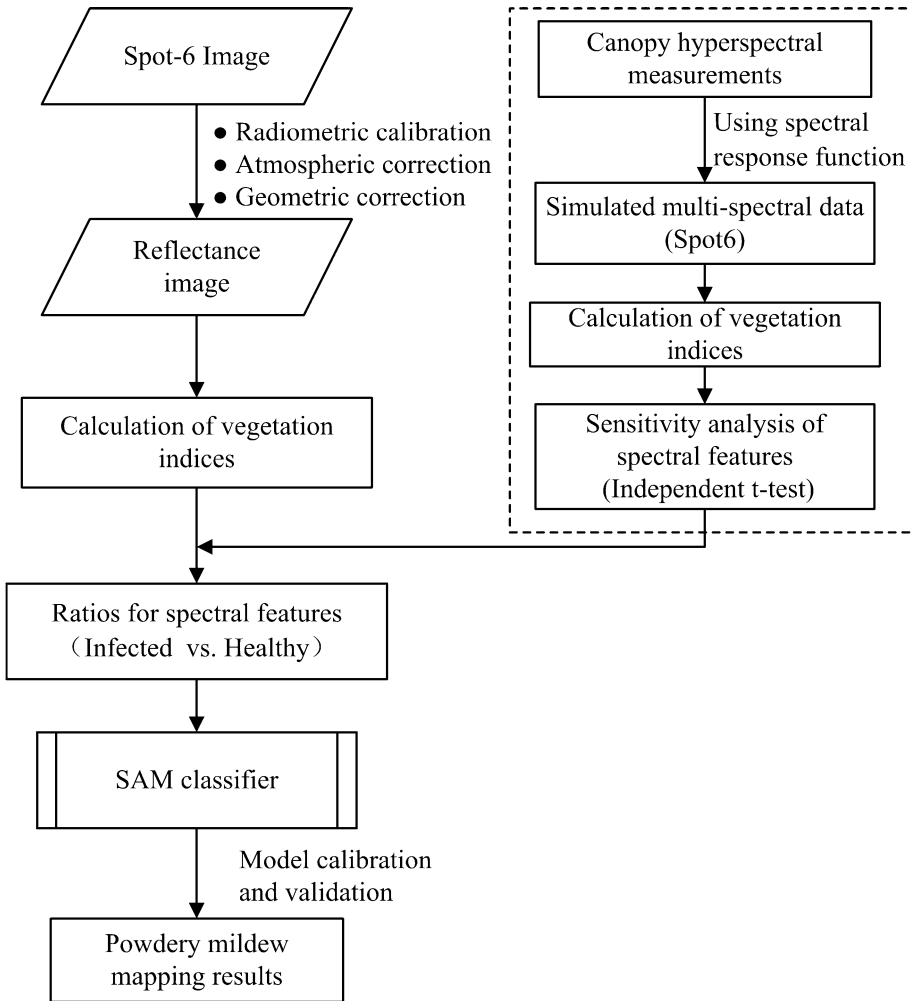


**Fig. 1** A workflow of mapping powdery mildew at a regional scale

growing season, the powdery mildew occurred naturally in the experimental field. A gradient of disease severity was generated in a field through a variable rate of fungicide application.

The field survey was conducted in a disease outbreak region in Mei county of Shaanxi province, China (34°2'12.86"N, 107°0'48.84"E) (Fig. 2). Mei county is located near Qin mountain that is an important geographical boundary to differentiate southern and northern China. Warm and humid climate characteristics in the study area with a relatively high elevation enable the over-summering and over-wintering of the powdery mildew pathogen, which makes Mei county a susceptible district to the disease in Shaanxi Province. In spring 2013, the powdery mildew occurred widely in Mei county. Within Mei county, two regions consisting of big wheat parcels were chosen as the study area for disease mapping (see Fig. 2).

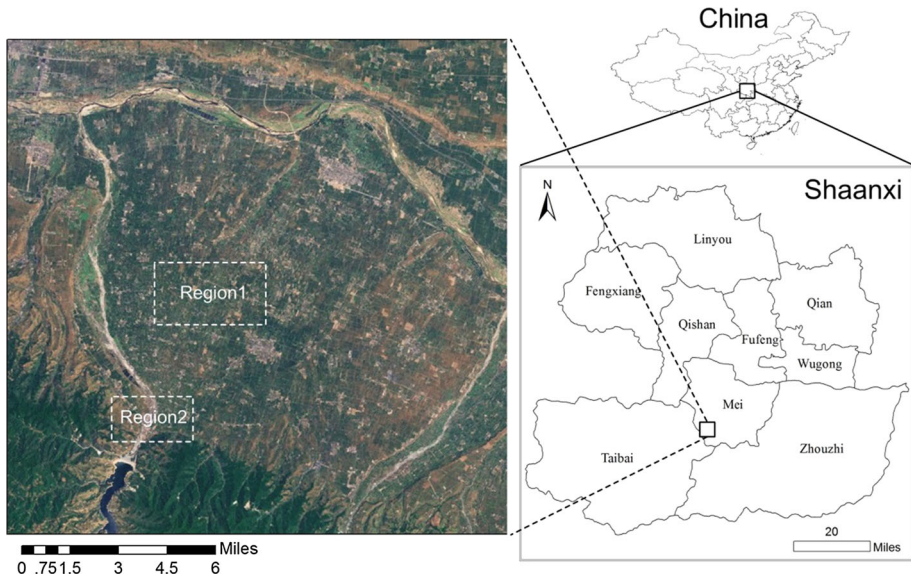


**Fig. 2** A map of survey points in the study area in Shaanxi Province, P. R. China

## Experimental design and data acquisition

### *Canopy spectral measurements*

Canopy spectral measurements were taken by a FieldSpec<sup>®</sup> UV/VNIR spectro-radiometer (ASD Inc., Boulder, Colorado, USA) at 0.6 m above the canopy with a field of view of 23°. The spectra from wavelengths 400–2500 nm were collected by the spectro-radiometer. All measurements were taken under clear sky conditions and only between 10:00 and 14:00 local time. The spectrum of a white spectralon reference panel was taken every ten canopy measurements in order to eliminate the effect of possible variation of illumination. For each measurement, fifteen readings were made and then averaged to obtain one spectrum. Given that the early grain filling stage is critical for prevention of powdery mildew, a total of 56 canopy spectra were measured at this stage. Those samples covered different infection status, including seven spectra of healthy canopies (no visible symptoms on leaves could be seen), 32 spectra of lightly infected canopies (lesions covered less than 50 % of the leaf on average) and 17 spectra of seriously infected canopies (lesions covered over 50 % of the leaf on average). Figure 3 provides nadir views of both healthy and infected wheat canopies.

### *Image acquisition and field survey*

A SPOT-6 image was acquired on May 11, 2013 over the study area, concurring with the early grain filling stage when powdery mildew manifested the most distinct symptoms in the field. Along with the image acquisition, an intensive field survey was carried out within the study area at the same time, providing necessary calibration and validation data for the disease mapping. In the study area, given that the disease occurrence tended to appear to be



**Fig. 3** Photos of healthy and powdery mildew infected winter wheat canopies

relatively homogeneous in the field, a simple yes/no criterion was applied in the field survey. Along with the image acquisition, a field survey was carried out at the same time at 37 plots in region 1 (19 healthy and 18 infected plots) and 19 plots in region 2 (10 healthy and 9 infected plots). At each plot with a size of 6 m × 6 m (the same as pixel size of SPOT-6 image), disease occurrence was checked. At the center of each plot, its geolocation was measured by using a Trimble GeoXT DGPS with sub-meter accuracy. The distribution of all surveyed plots is shown in Fig. 4.

## Data processing

### *Canopy spectral processing*

To assess the suitability of SPOT-6 for disease monitoring, an integration procedure was applied to the hyperspectral data based on a RSR function of the SPOT-6 sensor. For this case, the narrow band hyperspectral spectrum was converted to a broad band multi-spectral spectrum. The integration was done by:

$$R = \int_{r_{-\lambda 1}}^{r_{-\lambda n}} f(r) dr \quad (1)$$

where  $R$  is the simulated reflectance of a certain channel of the multi-spectral sensor;  $r$  is the reflectance at a hyperspectral wavelength;  $r_{-\lambda 1}$  and  $r_{-\lambda n}$  indicate reflectance of the beginning and ending wavelengths of this channel, respectively, and  $f(\lambda)$  represents the corresponding RSR function of the multi-spectral sensor (i.e., SPOT-6 in this study).

### *Image data processing*

The SPOT-6 image was rectified to the Universal Transverse Mercator (UTM), World Geodetic Survey 1984 (WGS-84), Zone 48, co-ordinate system. The image preprocessing



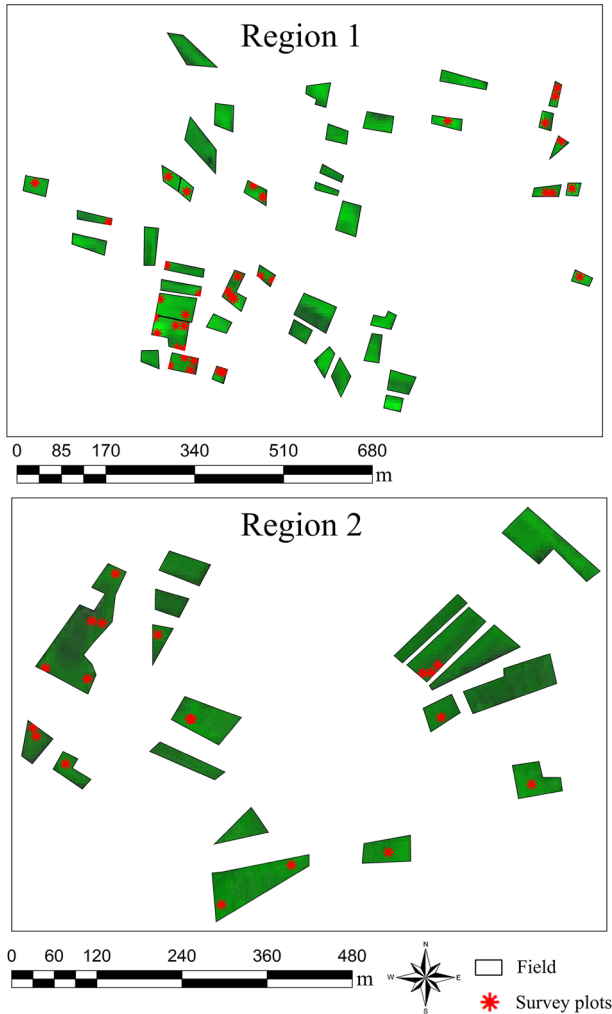


**Fig. 4** Distribution of survey plots on wheat field parcels for both regions. The SPOT-6 image with a false color combination as R/G/B = Green/NIR/Red bands was used as the background image

included a radiometric calibration, an atmospheric correction and a geometric correction (Liang et al. 2001). The calibration coefficients were first obtained from the header file of the original image data. The calibrated data were then processed for an atmospheric correction with the algorithm provided by Liang et al. (2001), which estimated the spatial distribution of atmospheric aerosols and retrieved surface reflectance under general atmospheric and surface conditions. Finally, a geometric registration was conducted against a set of ground control points ( $n = 56$ ) that were collected with a sub-meter-accuracy differential global positioning system (DGPS) device [Trimble GeoXT, (Sunnyvale, CA, USA)]. The root mean square error (RMSE) for the geometric-corrected image was less than half a pixel size (3 m). Given that the spectral difference between infected and healthy wheat plants was relatively smaller than spectral difference between different ground cover types (e.g., water, vegetation, impervious area), it is necessary to mask out

the wheat planted area prior to disease monitoring. To do so, a visual interpretation was implemented to extract boundaries of wheat parcels from the panchromatic layer of SPOT-6 imagery (Fig. 4).

### *Spectral features and sensitivity analysis*

In addition to using the four original bands of SPOT-6, the sensitivity of seven vegetation indices to powdery mildew was also examined. The seven VIs included normalized difference vegetation index (NDVI), green normalized difference vegetation index (GNDVI), triangular vegetation index (TVI), soil adjusted vegetation index (SAVI), atmospherically resistance vegetation index (ARVI), enhanced vegetation index (EVI) and re-normalized difference vegetation index (RDVI). Some of these VIs have been demonstrated to be responsible for the plant stress status, such as NDVI and TVI (Zhao et al. 2004; Naidu et al. 2009). The other VIs (i.e., GNDVI) were also used for detecting plant diseases (Zhao et al. 2004; Naidu et al. 2009; Yang et al. 2007). The definition, calculation formulae and references for the seven VIs are summarized in Table 2.

To evaluate the sensitivity of the candidate spectral features (SFs) to powdery mildew, a two-step selection principle was adopted, including an independent *t* test analysis and a cross-correlation check. Firstly, the independent *t* test was applied to examine whether the difference of a SF between healthy and infected samples was statistically significant at a significance level ( $\alpha = 0.05$ ). The *t*-test analysis was implemented on both simulated spectral data and real satellite image spectral data. Only SFs extracted from both data sets that all exhibited sensitivity to the disease were retained. Furthermore, to eliminate the redundant information among SFs, a cross-correlation check was conducted. For a SF pair that has high correlation with  $R^2 > 0.8$ , the one with relatively low disease sensitivity would be dropped. By traversing all combinations of SFs with this procedure, it was guaranteed that the redundancy among the retained SFs was relatively low. And only retained SFs were used for further model development.

### *SAM algorithm for disease mapping*

To map the disease with the retained SFs, a supervised classification algorithm, the spectral angle mapper (SAM) was used in this study. It transforms the responses of a pixel in the different bands into a vector in a space of *n* dimensions, where *n* is the number of bands in the multi-spectral image. The SAM compares the angle between the endmember spectrum vector and each pixel vector. In this way, an unknown pixel will be assigned to a class (i.e., either healthy or infected class in this study) with a highest similarity measured by an angle distance (Kruse et al. 1993). A formula of *n*-dimensional angle can be written as:

$$\theta = \arccos \frac{\sum_{i=1}^L x_i y_i}{\sqrt{\sum_{i=1}^L x_i^2} \sqrt{\sum_{i=1}^L y_i^2}}, \theta \in \left[0, \frac{\pi}{2}\right] \quad (2)$$

where *L* is the number of the selected spectral features; *x* is the corrected spectral feature vector for a reference pixel (i.e., healthy and infected), and *y* is the corrected spectral feature vector for a test pixel. In this method, to eliminate possible baseline effects across different regions, a spectral correction was processed on the selected features. The



**Table 2** A summary of spectral vegetation indices that were used for detection of powdery mildew

Title	Definition	Formula	Literature
$R_B$	Original reflectance of each band of SPOT-6		
$R_G$			
$R_R$			
$R_{NIR}$			
NDVI	Normalized difference vegetation index	$(R_{NIR} - R_R)/(R_{NIR} + R_R)$	Rouse et al. 1973
GNDVI	Green normalized difference vegetation index	$(R_{NIR} - R_G)/(R_{NIR} + R_G)$	Gitelson et al. 1996
TVI	Triangular vegetation index	$0.5[120(R_{NIR} - R_G) - 200(R_R - R_G)]$	Brogeand Leblanc 2001
SAVI	Soil adjusted vegetation index	$(1 + L) * (R_{NIR} - R_R)/(R_{NIR} + R_R + L)$ ; $L = 0.5$	Huete 1988
ARVI	Atmospherically resistance vegetation index	$R_{NIR} - (2R_R - R_B)/R_{NIR} + (2R_R - R_B)$	Kaufman and Tanre 1992
EVI	Enhanced vegetation index	$2.5(R_{NIR} - R_R)/(R_{NIR} + 6R_R - 7.5R_B + 1)$	Huete et al. 2002
RDVI	Re-normalized difference vegetation index	$(R_{NIR} - R_R)/(R_{NIR} + R_R)^{0.5}$	Roujean and Breon 1995

correction was implemented by multiplying the original SF by a correction coefficient, which is actually a spectral ratio of infected to healthy samples. The corrected SF can be calculated by:

$$SF_{corrected} = SF \frac{\overline{SF_{infected}}}{\overline{SF_{healthy}}} \quad (3)$$

where  $SF$  is the original spectral feature;  $SF_{corrected}$  is the corrected spectral feature;  $\overline{SF_{healthy}}$  and  $\overline{SF_{infected}}$  represent the average value of known healthy ( $n = 10$ ) and infected samples ( $n = 6$ ) as references, which were randomly selected from the field survey data. Then, based on corrected SFs, the disease mapping model was established using a SAM method, which was processed in ENVI 4.8 (ENVI4.8 2012).

For an accuracy assessment, a confusion matrix was generated from all the field survey samples except those used for reference samples. The accuracy indices including overall accuracy (OA), producer's accuracy, user's accuracy and kappa coefficient were used for assessing the disease mapping accuracy (Congalton 1991).

## Results and discussion

### Spectral signatures of powdery mildew canopies

The spectral reflectance curves of both infected and healthy canopies and their ratio curves, as shown in Fig. 5, allow a straightforward understanding of spectral variation that was induced by powdery mildew infection. Generally, the powdery mildew infection can increase reflection in the VIS region and decrease reflectance in the NIR region. In the ratio curves, there were two peaks in the VIS region around 490 and 670 nm, respectively, where healthy and diseased samples have the largest spectral difference (Fig. 5b). Comparing ratio curves between slightly infected canopies and seriously infected canopies, it is noticeable that with increase of infection severity, the reflectance ratio curve tends to exhibit a steeper shape in the VIS region and a more significant decrease in the NIR region. In this study relative to healthy canopy, in the VIS region, the largest reflectance was increased by 46.3 and 53.8 % whereas, in the NIR region, the largest reflectance was decreased by 7.6 and 13.7 % for slightly and heavily infected canopies, respectively.

There is a common doubt as to whether broad-band sensors are capable of capturing spectral signatures of plant diseases that might be always obvious in narrow bands. By overlapping the wavelength ranges of four SPOT-6 channels on the reflectance ratio curves of powdery mildew, it is encouraging to observe that those disease sensitive regions (characterized by concave-convex shape in the canopy reflectance ratio curves) were just located by the four SPOT-6 channels (Fig. 5b). Such observation indicates that the band setting of SPOT-6 might have a potential to capture spectral response of powdery mildew. Such a finding was in a good agreement with the study by Zhang et al. (2012), which suggested that powdery mildew could be detected by multi-spectral data. More quantitative analysis about the capability of SPOT-6 data in disease mapping is addressed in the following sections.

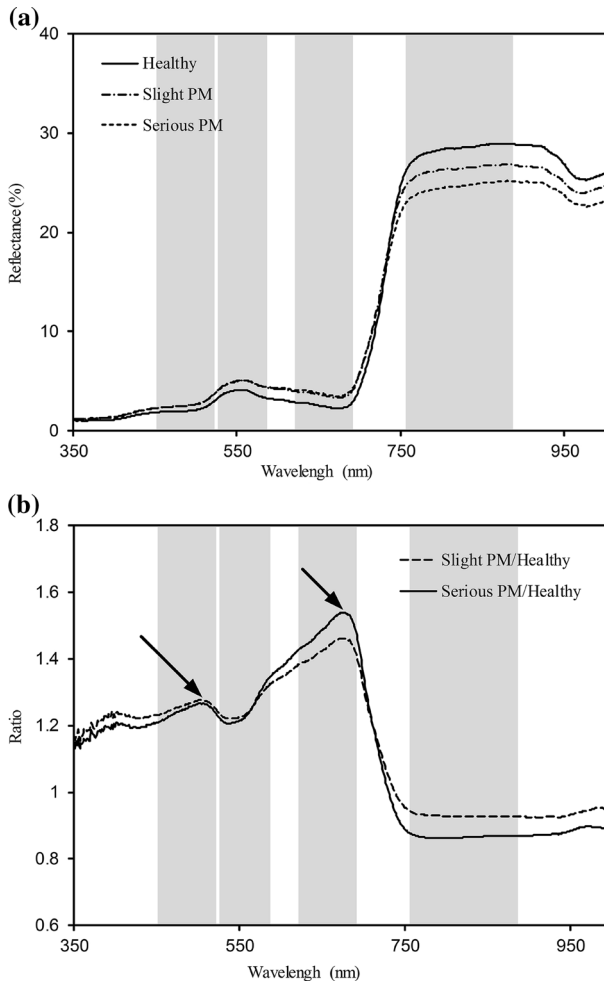


**Fig. 5** Original spectral reflectance (a) and spectral ratios of infected to healthy winter wheat (b). The grey color blocks indicate the spectral regions of the four SPOT-6 bands

### Sensitivity of spectral features to powdery mildew infection

All spectral features were examined for their response to powdery mildew using an independent t-test. The SFs were constructed with both simulated spectral data from canopy hyperspectral measurements and real satellite image spectral data. Table 3 summarizes the sensitivity levels of all SFs. The sensitivity testing results suggested that the response of most SFs to powdery mildew except NIR band were statistically significant. The insignificant response of the NIR band might be because many factors other than disease infection (e.g., planting density, leaf area index and canopy structure) would have led to variation of NIR reflectance. Generally, both simulated reflectance spectra and satellite image spectra derived SFs have shown a similar spectral response to powdery mildew (Table 3). However, there still exists a slight difference of sensitivity to powdery

**Table 3** A summary of disease sensitivity of spectral features

Spectral features	Independent <i>t</i> test		SFs selection	
	Simulative spectra	Real satellite image spectra	Independent <i>t</i> test	Cross-correlation check
Blue	**	***	○	
Green	**	*	○	○
Red	**	***	○	○
NIR				
NDVI	***	***	○	○
TVI	*	*	○	○
GNDVI	***	**	○	
SAVI	**	**	○	
ARVI	***	*	○	○
EVI	**			
RDVI	**	**	○	

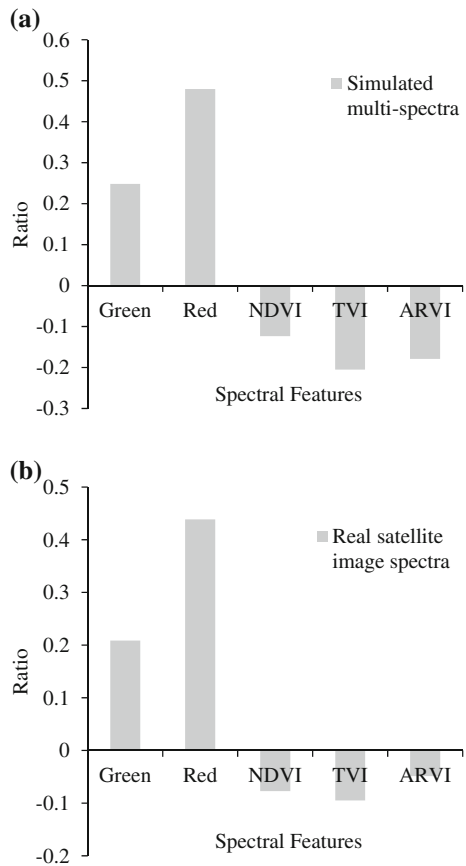
\* *p* value <0.05; \*\* *p* value <0.01; and \*\*\* *p* value <0.001; ○ SFs retained after independent *t* test analysis (selection step 1) and cross-correlation check (selection step 2), respectively

mildew between the two types of SFs. It is understandable that the atmospheric correction of a satellite image is unable to eliminate the atmospheric influence completely. Consequently, the remainder of atmospheric effect for the satellite image spectra might lead to slightly lesser sensitivity of some SFs to powdery mildew. Therefore, this factor together with some other possible errors in the measurement process (e.g., sensor configuration, calibration error, etc.) could have explained the slight difference of sensitive level of the SFs extracted from the two types of spectral data. As a strict feature identification process, only SFs derived from the two types of spectra (i.e., simulated and satellite image spectra) and with significant response (*p* value <0.05) to powdery mildew were retained. Finally, after eliminating a significantly redundant effect between SFs, a total of five SFs: green band, red band, NDVI, TVI and ARVI, were retained as the most ideal SFs, which would be used for subsequent disease mapping. Of the chosen spectral features, the two visible bands are associated with canopy color change due to disease infection. The NDVI is proven to be an efficient VI in reflecting a general physiological status of green plants (Rouse et al. 1973; Weng 2011). Variation of both pigment contents (mainly chlorophyll) and leaf area index would cause a corresponding response of NDVI to the powdery mildew. TVI provides an improved quantification of plant chlorophyll content more than NDVI by calculating a triangular spectral area in the visible domain, which has shown potential in detecting plant stress (Broge and Leblanc 2001). ARVI, with its advantage in suppressing the atmospheric effect, might be beneficial to disease mapping with satellite images.

### Mapping of powdery mildew with SAM model

The significant response of SFs derived from both simulated spectral data and real satellite image spectral data to the powdery mildew at canopy level illustrated the possibility of mapping powdery mildew with multi-spectral satellite images. As shown in Fig. 6, the ratio vectors derived from both satellite image spectra and simulated spectra exhibited a

**Fig. 6** Ratio bars consisting of the selected five spectral features extracted from both simulated multi-spectra (a) and real satellite image spectra (b)



similar pattern between Fig. 6a and b, suggesting that the spectral response to powdery mildew remains detectable in multi-spectral satellite image data. In addition, instead of using a single SF in disease mapping, multiple infection-sensitive SFs with a low redundancy were chosen to be used in disease mapping. This is mainly based on the fact that different stressors might cause similar spectral response as in a single SF, but are less likely to have similar spectral responses from multiple SFs simultaneously. Therefore, the ratio vector created from the multiple SFs represented a spectral signature of either powdery mildew infected or healthy pixel (sample). To apply this method in practice, users only need to provide a predefined ratio vector of a specific disease or mark several unique healthy and infected pixels as in this study, rather than to collect a dataset consisting of a gradient of disease severities (Yuan et al. 2014).

The mapping results for region 1 and region 2 by the SAM method were demonstrated in Fig. 7. Table 4 summarizes several classification accuracy indices of the mapping result after being validated against field survey samples. The SAM method produced a moderate accuracy with overall accuracy of 78 % and kappa coefficient of 0.55, as comparing with previous studies associated with disease mapping with high resolution satellite images (Franke and Menz 2007; Oumar and Mutanga 2012). By analyzing the confusion matrix, the misclassification from infected pixels to healthy pixels was the major error, which led

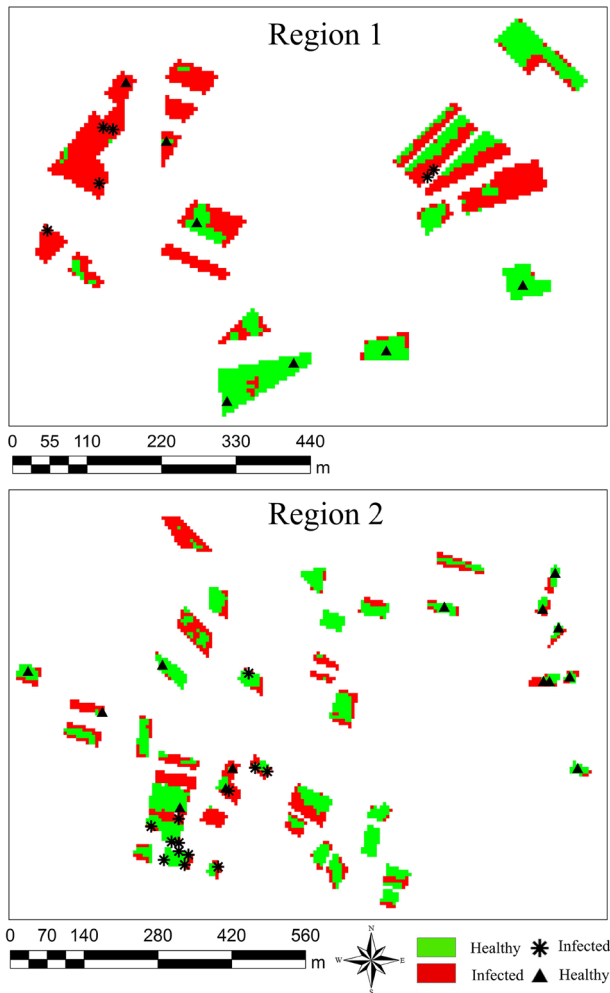


**Fig. 7** Mapping results of powdery mildew damage using the SAM method from the 5-band imagery

to a high omission error (31.58 %) and a relatively low commission error (18.75 %). Such misclassifications usually occur in samples with slight infection symptoms and particularly in fields with a high level of heterogeneity (Zhang et al. 2012; Cao et al. 2013). Unlike some data mining methods (e.g., artificial neural network, support vector machine) with complex principles, the SAM has an explicit physical basis and a straightforward computational scheme, which makes it efficient for disease mapping. SAM uses a classification decision rule based on spectral angles formed between a reference spectrum and unclassified test pixel spectrum in  $n$ -dimensional space. Such a clear principle fits well with this case in disease mapping. In this work, a set of disease sensitive spectral features constituted a spectral vector, which can indicate the most unique spectral variation of powdery mildew. The consistent spectral variation patterns that were found between in situ-based spectra and pixel-based spectra (Fig. 6) suggested that the spectral uniqueness of the disease maintained at image pixel level. Through calculating a spectral angle between a



**Table 4** Confusion matrix and classification accuracies calculated from a set of validation samples

	Reference			U.'s a. (%)	OA/AA (%)	Kappa	Commission error (%)
	Healthy	Diseased	Sum				
Classified							
Healthy	18	6	24	75.00	77.50/77.07	0.55	25.00
Diseased	3	13	16	81.25			18.75
Sum	21	19	40				
P.'s a. (%)	85.71	68.42					
Omission error (%)	14.29	31.58					

The classification result was created with the SAM classifier

*P.'s a.* producer's accuracy, *U.'s a.* user's accuracy, *OA* overall accuracy, *AA* average accuracy

reference spectrum and a test pixel spectrum, the SAM measures differences in spectral shape across selected spectral features, which is a straightforward way to reflect an overall spectral difference pattern between the reference and test pixel spectra.

Although the present accuracy (OA) was relatively lower than those achieved by using airborne hyperspectral imagery (Zhang et al. 2003; Yang et al. 2010), it is able to satisfy most practical needs in disease management for administration of plant protection (West et al. 2003). Using airborne hyperspectral imagery, the finer spectral resolution of hyperspectral data allows many detailed spectral analyses (e.g., extraction of red edge optical parameters and developing narrow band VIs), which might result in a certain improvement in mapping disease accuracy. Besides, as a successful example in mapping cotton root rot using high resolution satellite imagery by Yang et al. (2010), the significant spectral response and low heterogeneity in their experimental field might explain the reason responsible for their high accuracy (Yang et al. 2010).

In previous work by Zhang et al. (2014), authors used multi-temporal moderate resolution satellite images for mapping powdery mildew of winter wheat at a regional scale. The highest classification accuracy (78 %) was achieved by a relatively comprehensive strategy, which was linked to MTMF with PLSR. Despite using mono temporal satellite image only, a similar accuracy (78 %) was achieved in the present work, which might be owing to the improvement of spatial resolution from 30 m to 6 m. The consistent spectral responses to powdery mildew were found between in situ-based spectra and pixel-based spectra. Moreover, the SAM algorithm that was founded on a set of selected SFs was proven as a simple and effective classifier in disease mapping.

Although both studies in Zhang et al. (2014) and this paper have shown great potential in crop diseases mapping, the mapping accuracy was still somewhat insufficient in practice. To further improve the capability in emphasizing weak information (i.e., disease signal), satellite images that meet the requirements of both high spatial and temporal resolution are necessary. Moreover, some ancillary data, such as multi-temporal information, larger sample size, geographic data and even meteorological data, need to be included in the disease monitoring model to enhance the model performance.

## Conclusions

To map powdery mildew in winter wheat from the point of view of practical application, a newly launched high spatial resolution multi-spectral imaging sensor, SPOT-6, was tested over an area with natural disease occurrence in Mei county, Shaanxi province, China. Several conclusions could be drawn from the experimental results: (1) A consistent and unique spectral response of five selected spectral features to powdery mildew disease in winter wheat plants by analyzing both in situ-based spectra and pixel-based spectra indicated that the disease could be detected by broadband multi-spectral satellite image data; (2) a spectral ratio analysis facilitated a robust performance of a mapping method; (3) the SAM classification underlying a set of selected spectral features achieved a promising performance, which thus was considered as a simple but effective classifier in disease mapping.

**Acknowledgments** This work was subsidized by National Natural Science Foundation of China (41301476), Beijing Nova Programme, China (Z151100000315059), and UK Newton project entitled “A system to improve the rational use of pesticides against locusts”. The authors are grateful to Mr. Weiguo Li, Ms. Hong Chang for their helps in field data collection.

## References

- Broge, N. H., & Leblanc, E. (2001). Comparing prediction power and stability of broadband and hyperspectral vegetation indices for estimation of green leaf area index and canopy chlorophyll density. *Remote Sensing of Environment*, 76(2), 156–172.
- Calderón, R., Navas-Cortés, J. A., Lucena, C., & Zarco-Tejada, P. J. (2013). High-resolution airborne hyperspectral and thermal imagery for early detection of *Verticillium* wilt of olive using fluorescence, temperature and narrow-band spectral indices. *Remote Sensing of Environment*, 139, 231–245.
- Cao, X., Luo, Y., Zhou, Y., Duan, X., & Cheng, D. (2013). Detection of powdery mildew in two winter wheat cultivars using canopy hyperspectral reflectance. *Crop Protection*, 45, 124–131.
- Congalton, R. G. (1991). A review of assessing the accuracy of classifications of remotely sensed data. *Remote Sensing of Environment*, 37, 35–46.
- ENVI4.8. (2012). ITT Visual Information Solutions, Boulder, CO. [www.itvis.com](http://www.itvis.com).
- Franke, J., & Menz, G. (2007). Multi-temporal wheat disease detection by multi-spectral remote sensing. *Precision Agriculture*, 8(3), 161–172.
- Gitelson, A. A., Kaufman, Y. J., & Merzlyak, M. N. (1996). Use of green channel in remote sensing of global vegetation from EOS-MODIS. *Remote Sensing of Environment*, 58(3), 289–298.
- Hicke, J. A., & Logan, J. (2009). Mapping whitebark pine mortality caused by a mountain pine beetle outbreak with high spatial resolution satellite imagery. *International Journal of Remote Sensing*, 30(17), 4427–4441.
- Huang, W. J., Lamb, D. W., Niu, Z., Zhang, Y., Liu, L. Y., & Wang, J. H. (2007). Identification of yellow rust in wheat using in situ spectral reflectance measurements and airborne hyperspectral imaging. *Precision Agriculture*, 8(4), 187–197.
- Huete, A. R. (1988). A soil-adjusted vegetation index (SAVI). *Remote Sensing of Environment*, 25(3), 295–309.
- Huete, A. R., Didan, K., Miura, T., Rodriguez, E. P., Gao, X., & Ferreira, L. G. (2002). Overview of the radiometric and biophysical performance of the MODIS vegetation indices. *Remote Sensing of Environment*, 83(1), 195–213.
- Kaufman, Y. J., & Tanre, D. (1992). Atmospherically resistant vegetation index (ARVI) for EOS-MODIS. *IEEE Transactions on Geoscience and Remote Sensing*, 30(2), 261–270.
- Kruse, F. A., Lefkoff, A. B., Boardman, J. W., Heidebrecht, K. B., Shapiro, A. T., Barloon, J. P., et al. (1993). The spectral image processing system (SIPS): Interactive visualization and analysis of imaging spectrometer data. *Remote Sensing of Environment*, 44(2–3), 145–163.
- Lee, W. S., Alchanatis, V., Yang, C., Hirafuji, M., Moshou, D., & Li, C. (2010). Sensing technologies for precision specialty crop production. *Computers and Electronics in Agriculture*, 74(1), 2–33.

- Liang, S. L., Fang, H. L., & Chen, M. Z. (2001). Atmospheric correction of Landsat ETM+ land surface imagery-Part1: Methods. *IEEE Transactions on Geoscience and Remote Sensing*, 39(11), 2490–2498.
- Mahlein, A., Oerke, E., Steiner, U., & Dehne, H. W. (2012). Recent advances in sensing plant diseases for precision crop protection. *European Journal of Plant Pathology*, 133(1), 197–209.
- Moshou, D., Bravo, C., Oberti, R., West, J. S., Ramon, H., Vougioukas, S., et al. (2011). Intelligent multi-sensor system for the detection and treatment of fungal diseases in arable crops. *Biosystems Engineering*, 108(4), 311–321.
- Naidu, R. A., Perry, E. M., Pierce, F. J., & Mekuria, T. (2009). The potential of spectral reflectance technique for the detection of Grapevine leafroll-associated virus-3 in two red-berried wine grape cultivars. *Computers and Electronics in Agriculture*, 66(1), 38–45.
- Oumar, Z., & Mutanga, O. (2012). Using WorldView-2 bands and indices to predict bronze bug (*Thaumastocoris peregrinus*) damage in plantation forests. *International Journal of Remote Sensing*, 34(6), 2236–2249.
- Roujean, J. L., & Breon, E. M. (1995). Estimating PAR absorbed by vegetation from bidirectional reflectance measurements. *Remote Sensing of Environment*, 51(3), 375–384.
- Rouse, J.W., Haas, R.H., Schell, J.A., & Deering, D.W. (1973). Monitoring vegetation systems in the Great Plains with ERTS. *Third ERTS Symposium, NASA SP-351*, NASA, Washington, DC, (Vol. 1, pp. 309–317).
- Sankaran, S., Mishra, A., Ehsani, R., & Davis, C. (2010). A review of advanced techniques for detecting plant diseases. *Computers and Electronics in Agriculture*, 72, 1–13.
- Wang, X., Zhang, M., Zhu, J., & Geng, S. (2008). Spectral prediction of *Phytophthora infestans* infection on tomatoes using artificial neural network (ANN). *International Journal of Remote Sensing*, 29(6), 1693–1706.
- Weng, Q. H. (2011). Advances in environmental remote sensing, Chapter 5. In R. L. Pu & P. Gong (Eds.), *Hyperspectral remote sensing of vegetation bioparameters*. Boca Raton: CRC Press.
- West, J. S., Bravo, C., Oberti, R., Lemaire, D., Moshou, D., & McCartney, H. A. (2003). The potential of optical canopy measurement for targeted control of field crop diseases. *Annual review of Phytopathology*, 41, 593–614.
- Yang, C. M., Cheng, C. H., & Chen, R. K. (2007). Changes in spectral characteristics of rice canopy infested with brown planthopper and leafhopper. *Crop Science*, 47(1), 329–335.
- Yang, C., Everitt, J. H., & Fernandez, C. J. (2010). Comparison of airborne multi-spectral and hyperspectral imagery for mapping cotton root rot. *Biosystems Engineering*, 107, 131–139.
- Yuan, L., Zhang, J. C., Shi, Y. Y., Nie, C. W., Wei, L. G., & Wang, J. H. (2014). Damage mapping of powdery mildew in winter wheat with high resolution satellite image. *Remote sensing*, 6(5), 3611–3623.
- Zhang, J. C., Pu, R. L., Wang, J. H., Huang, W. J., Yuan, L., & Luo, J. H. (2012). Detecting powdery mildew of winter wheat using leaf level hyperspectral measurements. *Computers and Electronics in Agriculture*, 85, 13–23.
- Zhang, J. C., Pu, R. L., Yuan, L., Wang, J. H., Huang, W. J., & Yang, G. J. (2014). Monitoring powdery mildew of winter wheat by using moderate resolution multi-temporal satellite imagery. *PLoS One*, 9(4), e93107.
- Zhang, M., Qin, Z., Liu, X., & Ustin, S. L. (2003). Detection of stress in tomatoes induced by late blight disease in California, USA, using hyperspectral remote sensing. *International Journal of Applied Earth Observation and Geoinformation*, 4, 295–310.
- Zhao, C. J., Huang, M. Y., Huang, W. J., Liu, L. Y., & Wang, J. H. (2004). Analysis of winter wheat stripe rust characteristic spectrum and establishing of inversion models. In: R. King & M. Datcu (Eds.), In *Proceedings of Geoscience and Remote Sensing Symposium* (Vol. 6, pp. 4318–4320). Alaska.